Contents lists available at ScienceDirect

Materials Characterization

Review

Microstructure and hot deformation behavior of the Cu-Sn-Ni-Zn-Ti (-Y) alloy

Deye Xu [a], Meng Zhou [a,b,c,*], Yi Zhang [a,b,c,*], Shunlong Tang [a], Zhiyang Zhang [a], Yong Liu [a,b,c], Baohong Tian [a,b,c], Xu Li [d], Yanlin Jia [e], Alex A. Volinsky [f], De Li [a], Qiujie Liu [a]

[a] School of Materials Science and Engineering, Henan University of Science and Technology, Luoyang 471023, PR China
[b] Provincial and Ministerial Co-construction of Collaborative Innovation Center for Non-ferrous Metals New Materials and Advanced Processing Technology, Henan Province, Luoyang 471023, PR China
[c] Henan Province Key Laboratory of Nonferrous Materials Science and Processing Technology, Luoyang 471023, PR China
[d] Center for Advanced Measurement Science, National Institute of Metrology, Beijing 100029, PR China
[e] College of Materials Science and Engineering, Central South University, Changsha 410083, PR China
[f] Department of Mechanical Engineering, University of South Florida, 4202 E. Fowler Ave. ENG 030, Tampa 33620, USA

ABSTRACT

The effects of Y addition on the microstructure evolution in the Cu-Sn-Ni-Zn-Ti alloys during hot deformation were investigated. The hot deformation experiments were carried out using a Gleeble-1500 simulator and the Cu-Sn-Ni-Zn-Ti and Cu-Sn-Ni-Zn-Ti-Y alloys deformed at 550–950 °C with 0.001–10 s^{-1} strain rate. The constitutive equations were constructed, and the hot deformation activation energy of the two alloys was calculated. Based on the true stress-strain curves and electron backscattered diffraction image analysis, it was concluded that the addition of 0.1 wt% rare earth Y element can promote dynamic recrystallization. The pole figures demonstrated the texture change from {011}⟨112⟩ Brass texture and {001}⟨100⟩ Cube texture to {111}⟨211⟩ R texture after Y addition. The microstructure and precipitates of the Cu-Sn-Ni-Zn-Ti alloy were analyzed by transmission electron microscopy, and Cu$_4$Ti precipitates were present in the alloy. The continuous dynamic recrystallization and the discontinuous dynamic recrystallization were the two main recrystallization mechanisms of the Cu-Sn-Ni-Zn-Ti alloy.

1. Introduction

Due to excellent mechanical properties, thermal conductivity, and corrosion resistance, copper alloys are widely used in aerospace, electronics, machinery manufacturing, and communications, and have become indispensable materials for social development. With the progress in science and technology, traditional materials can no longer meet the growing needs of high-tech industries, requiring better comprehensive performance [1–5]. Cu-Ni-Sn alloys can compensate for the shortcomings of traditional Cu-Be alloys in terms of better thermal stability, high-temperature strength and resistance to high-temperature stress relaxation, and no toxic emissions during production, making them popular environmentally friendly materials [6]. However, due to the large differences in melting point of Cu, Ni, and Sn (Cu: 1083 °C, Ni: 1453 °C, Sn: 232 °C), severe segregation can occur during melting and solidification of the alloy, and Sn segregation can lead to a large number

of defects in the alloy, making it prone to cracking during hot working and degrading its mechanical properties [7]. Many scholars have improved the preparation process of Cu-Ni-Sn alloys and addressed the adverse effects of segregation in the alloy, including mechanical alloying, rapid solidification, powder metallurgy, and vacuum melting.

Cu-Ni-Sn alloy is a typical amplitude modulation decomposition strengthening alloy. It was developed in 1928 [8] by adding Ni to the Cu-Sn alloy, which improved performance primarily by age hardening. In the 1960s the Cu-Ni-Sn alloys became the main materials for lead frames due to their excellent strength and electrical conductivity [9,10], and they have been extensively studied since then. The Cu-Ni-Sn alloys' properties have been substantially improved by controlling the relative content of each component and adding other elements, allowing Cu-Ni-Sn alloys to serve in a variety of operating environments. In recent years, studies have confirmed that the addition of trace elements to the alloy can improve its overall performance because they dissolve in the lattice

---

causing lattice distortion and increasing the internal stress of the alloy. These trace elements are Fe [11], Ti [12], Mg [13], Cr [14], Co [15], Ce [16], Ni [17,18], and Y [19]. The addition of Ti to the alloy can refine the grain and improve the creep resistance of the alloy. Ti can also increase the alloy recrystallization temperature and improve its high-temperature performance. Wang et al. [20] found that the addition of Ti could improve the microstructure and strength of the c-BN/Cu-Ni-Sn-Ti filler metals, and when the Ti content in the filler metal was 10 wt%, the maximum tensile strength reached 105.1 MPa. When the Ti content exceeded 15 wt%, microcracks formed at the interface due to the increase in TiNi, CuTi, and Cu_3Ti_2 brittle phases and residual stresses, reducing the alloy's tensile strength. Wang et al. [21] found that the addition of an appropriate amount of Zn had a significant effect on the mechanical properties of the alloy in terms of increased yield strength, ultimate tensile strength, and elongation. Yang et al. [22] found that rare earth Y element could promote DRX nucleation and δ-Co_2Si precipitation. These nanoscale particles interact with dislocations during hot deformation, improve the deformation resistance and increase the hot deformation activation energy of the Cu-Co-Si alloy by about 8%.

Based on the above studies, Cu-Sn-Ni-Zn-Ti and Cu-Sn-Ni-Zn-Ti-Y alloys were designed and prepared to investigate the effects of Y on the recrystallization behavior and microstructure evolution during hot deformation. The thermal deformation experiments were carried out using the Gleeble-1500 simulator at 550–950 °C deformation temperatures and 0.001–10 s^{-1} strain rates. The changes in flow stress, microstructure, electron backscatter diffraction (EBSD) images, and hot deformation activation energy of the alloy after the addition of Y were compared. The microstructure, types, and distribution of precipitated phases in the Cu-Sn-Ni-Zn-Ti alloy were analyzed by transmission electron microscopy (TEM).

2. Experimental materials and procedures

Fig. 1(a) shows the materials' preparation flow chart. The raw materials selected for alloy smelting were 99% standard electrolytic cathode copper, pure tin, pure nickel, pure zinc, copper-45% titanium intermediate alloy, and pure yttrium. The Cu-Sn-Ni-Zn-Ti and Cu-Sn-Ni-Zn-Ti-Y alloys used in the experiments were prepared by vacuum smelting in a ZG-0.01-40-4 vacuum medium frequency induction furnace. Argon gas was passed during the melting process to prevent the entry of oxygen, and a deoxidizer was added to react with impurities and form oxides floating on the surface to prevent oxidation. First, the copper block was placed into the furnace and other intermediate alloys were added after melting. The pouring temperature for the experiment was set in the 1150–1250 °C range. Finally, the molten metal was poured into a graphite crucible (90 mm inner diameter, 20 mm thickness, and 190 mm height) for cooling. The ingot was removed from the

mold after cooling to room temperature. The riser and outer skin were cut off, and the next heat treatment was performed.

Table 1 shows the nominal and actual composition of the Cu-Sn-Ni-Zn-Ti and Cu-Sn-Ni-Zn-Ti-Y alloys. The ingots were held at 960 °C for 2 h for annealing treatment, and then some of the ingots were cut into Φ8 mm × 12 mm cylinders using electrical discharge machining. A small hole Φ1 mm × 2 mm was made in the center of the cylinder to fit the thermocouple into the specimen. The thermal deformation experiments were carried out using a Gleeble-1500 thermomechanical simulator at 550–950 °C and 0.001–10 s^{-1} strain rate. As seen in Fig. 1(b), the specimens were heated to the experimental temperature, held for 3 min, and then compressed to 55% of the total deformation, followed by immediate water quenching. The specimens were cut along the compression direction and the center position of uniform deformation was used for microstructure characterization. First, the prepared specimens were etched in 3.5 g $FeCl_3$, 5 ml HCl and 95 ml anhydrous ethanol solution, and the microstructure of the Cu-Sn-Ni-Zn-Ti and Cu-Sn-Ni-Zn-Ti-Y alloys were observed using CX40M optical microscope. Then, the etched specimens were mechanically and electrochemically polished for scanning electron microscopy (SEM) observations using the JSM-7800F electron microscope. Finally, Φ3 mm × 50 μm samples were ion thinned with Gatan 691 ion polisher, and the microstructure of the Cu-Sn-Ni-Zn-Ti and Cu-Sn-Ni-Zn-Ti-Y alloys was observed by the FEI Tecnai F30 transmission electron microscope (TEM).

3. Results

3.1. Flow stress

In order to investigate the effects of Y on the rheological stress of the alloys, the of the Cu-Sn-Ni-Zn-Ti and Cu-Sn-Ni-Zn-Ti-Y alloys were deformed at 0.001 s^{-1}, 0.01 s^{-1}, 0.1 s^{-1}, 1 s^{-1}, and 10 s^{-1} strain rates from 550 °C to 950 °C. The true stress-strain curves are plotted in Fig. 2. The alloy hot deformation process consists of the three stages: work hardening, dynamic recovery, and dynamic recrystallization [23], which are closely related to the deformation temperature and strain rate. The stress-strain curves show alternating wave-like stress changes, which are the result of the interaction between work hardening and dynamic recrystallization. The dynamic recrystallization process

Table 1
The nominal and analyzed composition of the alloys.

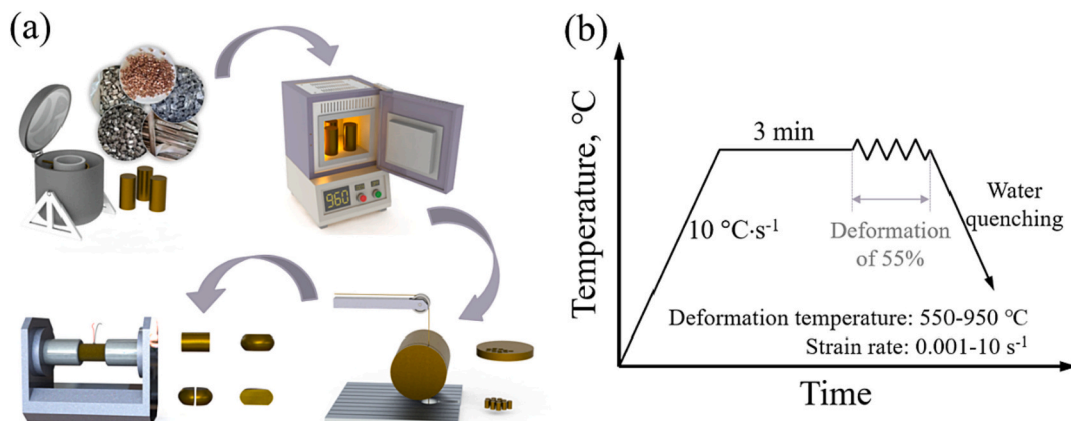| Nominal composition (wt%)	Analyzed composition (wt%)					
	Sn	Ni	Zn	Ti	Y	Cu
Cu-2Sn-1Ni-0.5Zn-0.25Ti	2.09	1.01	0.41	0.212	–	Bal.
Cu-2Sn-1Ni-0.5Zn-0.25Ti-0.15Y	1.95	0.968	0.49	0.22	0.1	Bal.

Fig. 1. Hot deformation experiments: (a) sample preparation process and (b) temperature profile.
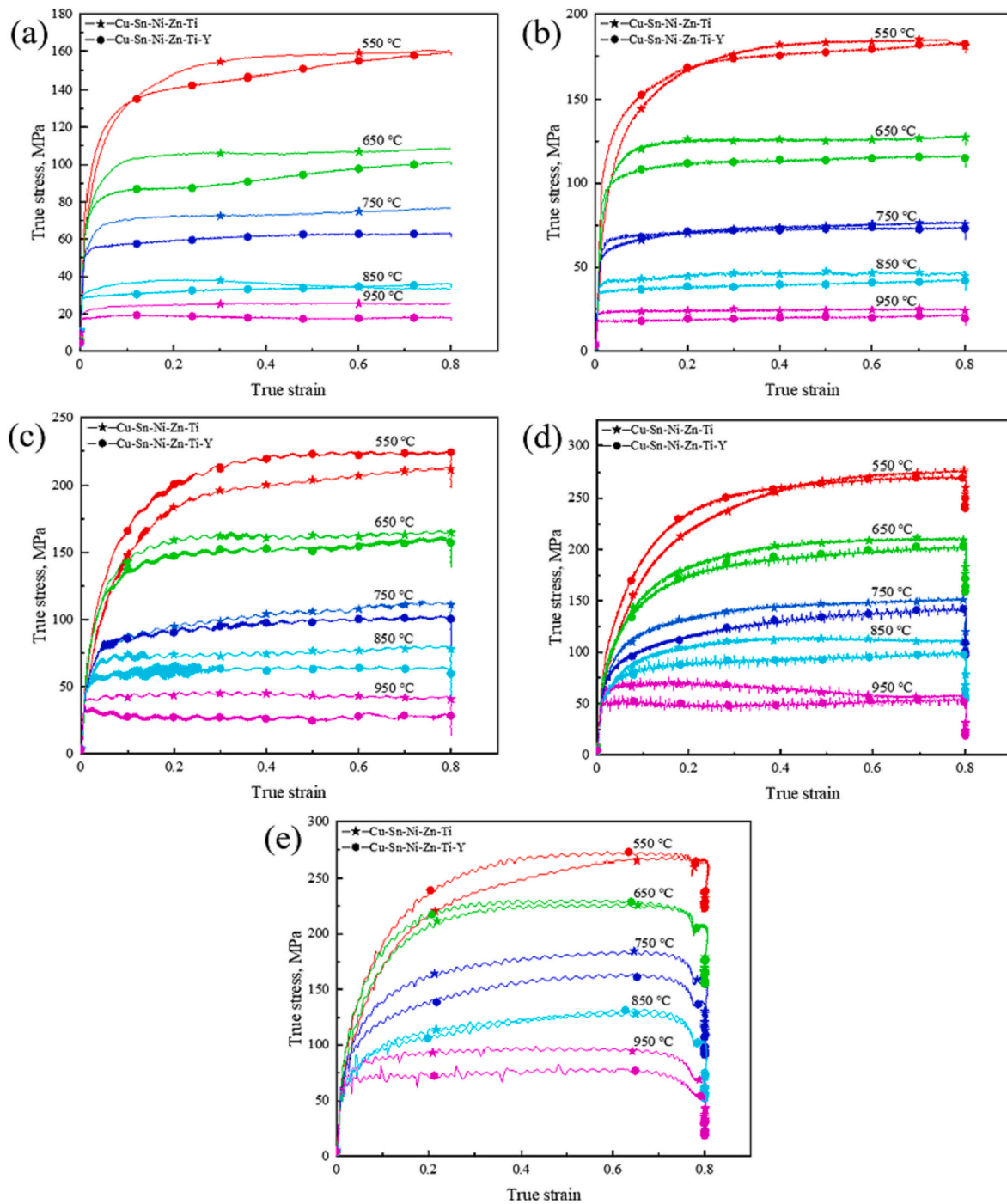
Fig. 2. True stress-true strain curves of the Cu-Sn-Ni-Zn-Ti and Cu-Sn-Ni-Zn-Ti-Y alloys deformed at (a) 0.001 s^{-1}, (b) 0.01 s^{-1}, (c) 0.1 s^{-1}, (d) 1 s^{-1}, and (e) 10 s^{-1} strain rates.

consumes dislocations and causes dynamic softening associated with the stress decrease. However, the dislocations slowly increase the stress, resulting in less driving force for recrystallization, and the softening effect of recrystallization weakens, process hardening regains dominance and the stress starts to rise. By the time the dislocation density re-accumulates, recrystallization again dominates and the stress is lowered again. This wave-like change process continues in similar cycles, but with a gradual decay in stress amplitude. The formation of recrystallized grains is the reason for the flow stress decrease [24], which explains the lower stress of the Cu-Sn-Ni-Zn-Ti-Y alloy after Y addition. When the alloy was deformed at a lower temperature of 550 °C and 0.01 s^{-1} strain rate, dislocation entanglement occurred due to grain slip, causing the

grains to be elongated, broken and fibrillated, and residual stresses were generated within the metal with increasing rheological stresses. At this time, work hardening dominates, thus increasing the stress in Fig. 2(b). When the deformation temperature of the alloy was 650–750 °C, the stress raised rapidly and then stabilized, indicating that the alloy has undergone work hardening and dynamic recovery during the compression process.

When the deformation temperature reaches 850–950 °C, the stress rises and then drops, which is an obvious dynamic recrystallization characteristic. Dynamic recrystallization consumes dislocations, and the increase in dislocation density due to work hardening provides favorable conditions for dynamic recrystallization [25]. Therefore, after the stress

reaches its peak, dynamic recrystallization dominates and the alloy undergoes dynamic softening, and the stress decreases.

3.2. Microstructure evolution

Fig. 3 shows the optical images of the Cu-Sn-Ni-Zn-Ti and Cu-Sn-Ni-Zn-Ti-Y alloys' microstructure under different deformation conditions. At lower deformation temperatures and strain rates, the internal distribution of the texture is not uniform, and the grains are compressed into long strips in the central part of the specimens, while they are still present as large grains in the edge regions. In Fig. 3(a) a large number of fine grains were observed at the grain boundaries of the Cu-Sn-Ni-Zn-Ti alloy deformed at 650 °C. This is due to the irregular arrangement of atoms at the grain boundaries during hot deformation and the presence of impurities that hinder dislocation movement and cause dislocation plugging, which provides the driving force for recrystallization nucleation. The fine recrystallized grains can be seen in the magnified view [26]. The microstructure of the Cu-Sn-Ni-Zn-Ti-Y alloy deformed at 650 °C and 0.01 s^{-1} strain rate is shown in Fig. 3(b). There are obvious fine recrystallized grains around the shear bands. The microstructure of the Cu-Sn-Ni-Zn-Ti and Cu-Sn-Ni-Zn-Ti-Y alloys deformed at 750 °C and 0.01 s^{-1} strain rate is shown in Fig. 3(c) and (d), respectively. A large number of recrystallized grains are present at grain boundaries. Dynamic recrystallization preferentially nucleates at grain boundaries and shear bands due to large strains at grain boundaries. The large strain at the grain boundaries provides the driving force for dynamic recrystallization nucleation [27]. Comparing the microstructure and the size of the newly generated recrystallized grains of the two alloys deformed at the same strain rate and different temperatures shows that the Y addition promotes the recrystallization of the alloy, which is consistent with the results of Yang et al. [22].

Fig. 4 shows the optical micrographs of the Cu-Sn-Ni-Zn-Ti and Cu-Sn-Ni-Zn-Ti-Y alloys deformed at 0.001 s^{-1} strain rate. Recrystallization preferentially occurs at grain boundaries and defects, and the recrystallized grains grow rapidly with temperature. Recrystallized grains in Fig. 4(d) and Fig. 3(d) are larger for the alloys deformed at
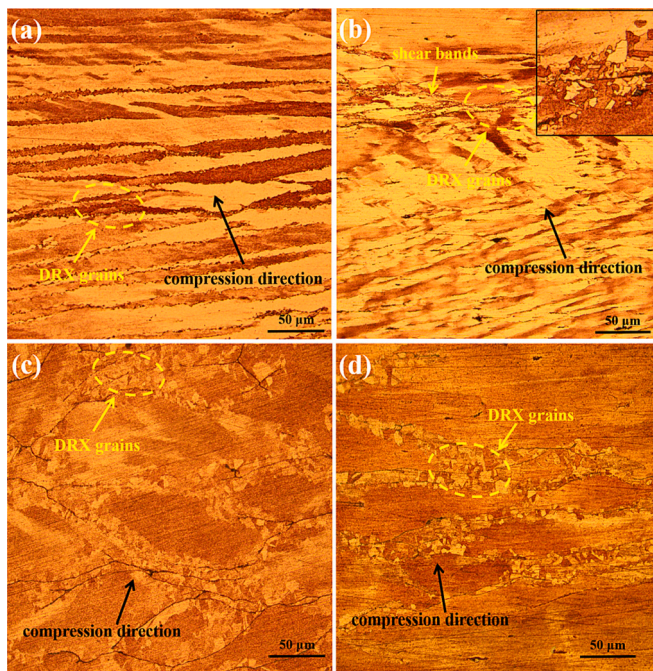

Fig. 4. The microstructure of the Cu-Sn-Ni-Zn-Ti and Cu-Sn-Ni-Zn-Ti-Y alloys deformed at 0.001 s^{-1} strain rate and different temperatures: (a) Cu-Sn-Ni-Zn-Ti 650 °C, (b) Cu-Sn-Ni-Zn-Ti-Y 650 °C, (c) Cu-Sn-Ni-Zn-Ti 750 °C, (d) Cu-Sn-Ni-Zn-Ti-Y 750 °C.
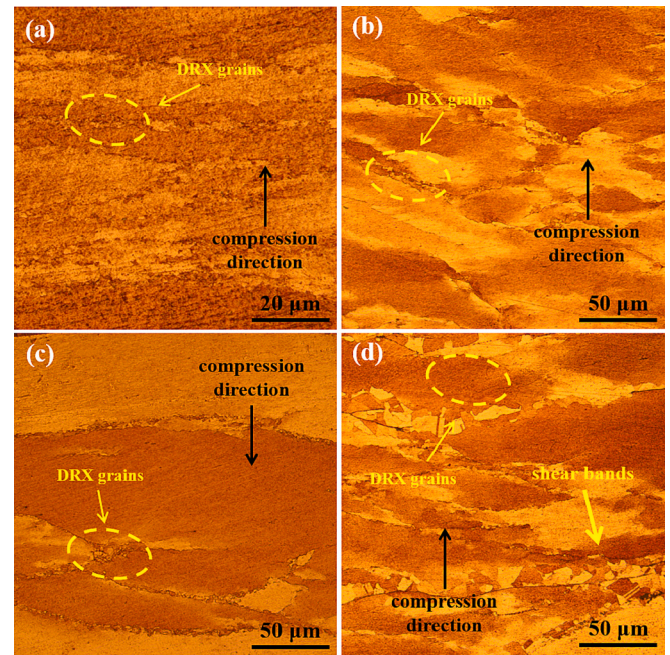
lower strain rates because the atoms have enough time for diffusion and grain boundary migration. It was verified again that the Y addition promoted the Cu-Sn-Ni-Zn-Ti alloy dynamic recrystallization.

3.3. Constitutive equations

In thermal processing, the hot deformation activation energy for hot deformation is the energy barrier that metal atoms need to cross during plastic deformation and is an important parameter for evaluating the thermal processing properties of alloys. Based on the experimental data of hot deformation, the constitutive equations were established and the hot deformation activation energy of the two alloys was calculated. The deformation temperature (T) and strain rate ($\dot{\varepsilon}$) are the two main factors affecting the flow stress (σ), and based on the Arrhenius equation, Sellars and McTegart [28] proposed a hyperbolic sine model:

$$\dot{\varepsilon} = A\left[\sinh(\alpha\sigma)^n \exp\left(-\frac{Q}{RT}\right)\right] \tag{1}$$

Eq. (1) can be expressed under different strain conditions as:

$$\dot{\varepsilon} = A_1\sigma^{n1}\exp\left[-\frac{Q}{RT}\right] \ (\alpha\sigma < 0.8) \tag{2}$$

$$\dot{\varepsilon} = A_2\exp(\beta\sigma)\exp\left[-\frac{Q}{RT}\right] \ (\alpha\sigma > 1.2) \tag{3}$$

Here, $\dot{\varepsilon}$ is the strain rate, σ is the peak stress, Q is the hot deformation activation energy, and T is the deformation temperature in K. A, A_1, A_2, α, β, n_1, n, and R are constants. Taking the natural logarithm of both sides of Eqs. (1–3) yields

$$\ln\dot{\varepsilon} = n\ln[\sinh(\alpha\sigma)] + \ln A - \frac{Q}{RT} \tag{4}$$

$$\ln\dot{\varepsilon} = n_1\ln\sigma + \ln A_1 - \frac{Q}{RT} \tag{5}$$

$$\ln\dot{\varepsilon} = \beta\sigma + \ln A_2 - \frac{Q}{RT} \tag{6}$$

Fig. 3. The microstructure of the Cu-Sn-Ni-Zn-Ti and Cu-Sn-Ni-Zn-Ti-Y alloys deformed at 0.01 s^{-1} strain rate and different temperatures: (a) Cu-Sn-Ni-Zn-Ti 650 °C, (b) Cu-Sn-Ni-Zn-Ti-Y 650 °C, (c) Cu-Sn-Ni-Zn-Ti 750 °C, (d) Cu-Sn-Ni-Zn-Ti-Y 750 °C.

Taking the partial derivative of Eq. (1) yields

$$Q = R\left[\frac{\partial(ln\dot{\varepsilon})}{\partial ln(\sin\alpha\sigma)}\right]_T \left[\frac{\partial ln(\sinh\alpha\sigma)}{\partial\left(\frac{1}{T}\right)}\right]_{\dot{\varepsilon}} = RnS \quad (7)$$

The effects of deformation conditions can be represented by the Zener-Hollomon parameter Z [29,30]:

$$Z = \dot{\varepsilon}exp\left[\frac{Q}{RT}\right] \quad (8)$$

Bringing Eq. (8) into Eq. (2) and taking the natural logarithm of both sides of the equation yields

$$lnZ = lnA + n[ln(\sinh(\alpha\sigma))] \quad (9)$$

The hot deformation activation energy of the Cu-Sn-Ni-Zn-Ti and Cu-Sn-Ni-Zn-Ti-Y alloys was calculated. Figs. 4(a-d) show the relationships between ln(strain rate) and lnσ, ln(strain rate) and σ, ln(strain rate) and ln[sinh(ασ)], ln[sinh(ασ)] and $T^{-1} \times 10^3$ K^{-1}, respectively. Here, n_1, β, n, and S correspond to the average values of the slopes in Fig. 5(a-d), respectively. For the Cu-Sn-Ni-Zn-Ti alloy, n_1 = 9.508 and β = 0.082, α = β/n_1 = 0.009, n = 6.497, and S = 5.091 were obtained. Similarly, for the Cu-Sn-Ni-Zn-Ti-Y alloy, n_1 = 10.177, β = 0.096, n = 7.271, and S = 5.065 were obtained. The hot deformation activation energy for hot deformation of the Cu-Sn-Ni-Zn-Ti and Cu-Sn-Ni-Zn-Ti-Y alloys was calculated as 274.855 kJ/mol and 307.757 kJ/mol, respectively. lnA is the intercept of Fig. 5(e), and according to Fig. 5(e) it can be derived that the intercepts of Cu-Sn-Ni-Zn-Ti and Cu-Sn-Ni-Zn-Ti-Y alloys are 29.607 and 33.422, respectively, so the values of A are $e^{29.607}$ and $e^{33.422}$, respectively. Therefore, the constitutive equations of the two alloys can
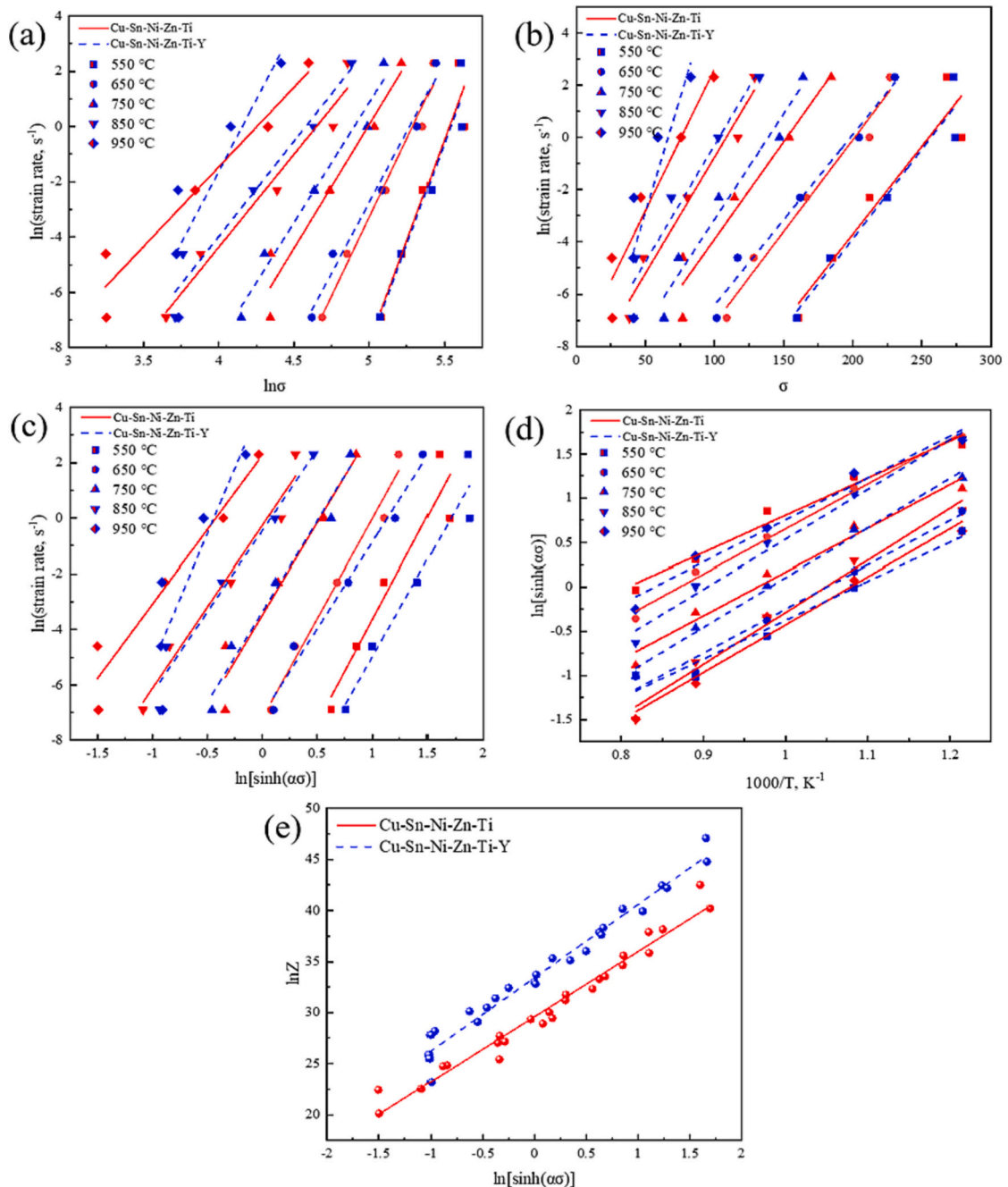

Fig. 5. Relations between: (a) lnε̇-lnσ, (b) lnε̇-σ, (c) lnε̇-ln[sinh(ασ)], (d) ln[sinh(ασ)]-1000/T, (e) lnZ-ln[sinh(ασ)].

be obtained for:

The Cu-Sn-Ni-Zn-Ti alloy:

$$\dot{\varepsilon} = e^{29.607}[sinh(0.009\sigma)]^{6.497} exp\left(-\frac{274,855}{RT}\right) \qquad (10)$$

The Cu-Sn-Ni-Zn-Ti-Y alloy:

$$\dot{\varepsilon} = e^{33.422}[sinh(0.009\sigma)]^{7.271} exp\left(-\frac{307,757}{RT}\right) \qquad (11)$$

The hot deformation activation energy of the Cu-Sn-Ni-Zn-Ti alloy increased by 12% after the addition of the rare earth Y element. This indicates that more energy is required for dynamic recrystallization and the dynamic recrystallization temperature increases, indicating that the Y addition results in better high-temperature stability of the copper alloy. Wang et al. [19] showed that the Y addition increases the hot deformation activation energy of the Cu-Mg alloy because it promotes the precipitation, and the precipitated phase pegs dislocations and grain boundaries and prevents dislocation movement, so higher hot deformation activation energy is obtained with the Y addition.

3.4. EBSD

To further investigate the effects of Y on the microstructure of the Cu-Sn-Ni-Zn-Ti alloys, the grain size, dislocation density, and weave transformations of the Cu-Sn-Ni-Zn-Ti and Cu-Sn-Ni-Zn-Ti-Y alloys after thermal deformation were analyzed by the EBSD technique. The inverse pole figure (IPF) maps of the Cu-Sn-Ni-Zn-Ti and Cu-Sn-Ni-Zn-Ti-Y alloys deformed at 0.01 s⁻¹ strain rate and different temperatures are shown in Fig. 6. According to Fig. 6(a) and (b), the grains are compressed into long strips during deformation at a lower temperature of 650 °C. A small number of fine recrystallized grains are generated around the coarse deformed grains, and recrystallization is only present at the grain boundaries due to the lower temperature. It can be judged that the alloy is in the initial stage of recrystallization. Recrystallization gradually starts to dominate with the increase of deformation

temperature. As seen in Fig. 6(c) and (d), a large number of recrystallized grains appear inside the alloy deformed at 750 °C. The grain growth is caused by the migration of high-angle grain boundaries, and the temperature is the main factor affecting grain boundary migration: the higher the temperature, the faster the grain growth rate. Increasing the deformation temperature promotes the recrystallization of the alloy. After the addition of Y, recrystallization spreads at the grain boundaries and the degree of recrystallization of the alloy is significantly increased. Therefore, it can be concluded that Y promotes the recrystallization of the Cu-Sn-Ni-Zn-Ti alloy.

The migration of high-angle grain boundaries is related to the dislocation density at the grain boundaries. In order to calculate the dislocation density inside the alloy, the kernel average misorientation (KAM) maps were plotted. Fig. 7 shows the KAM for the two alloys deformed at 650 °C and 750 °C with 0.01 s⁻¹ strain rate. The red region represents the high dislocation density and the blue region represents the low dislocation density. The geometrically necessary dislocation (GND) density is related to the kernel average misorientation as follows [31]:

$$\rho^{GND} = 2\theta/\mu b \qquad (12)$$

Here, ρ^{GND} is the geometrically necessary dislocation density in m⁻², θ is the average misorientation value in rad, μ is the 2.5 μm scan step, and b is the 0.255 nm Burgers vector.

Dislocation density has important effects on strength and toughness of metals [32]. Dislocations are usually stored at grain boundaries or crystal defects and provide the driving force for the nucleation of recrystallized grains. The calculated dislocation density at different temperatures was 8×10^{15} m⁻² and 6.9×10^{15} m⁻² for the Cu-Sn-Ni-Zn-Ti alloy and 7.7×10^{15} m⁻² and 4.8×10^{15} m⁻² for the Cu-Sn-Ni-Zn-Ti-Y alloy, respectively. The Cu-Sn-Ni-Zn-Ti-Y alloy has a lower dislocation density. Recrystallization is the main reason for dislocation consumption and lower dislocation density. The growth of dynamic recrystallization requires the energy stored in dislocations to provide the driving force. In other words, the addition of Y promotes alloy recrystallization.
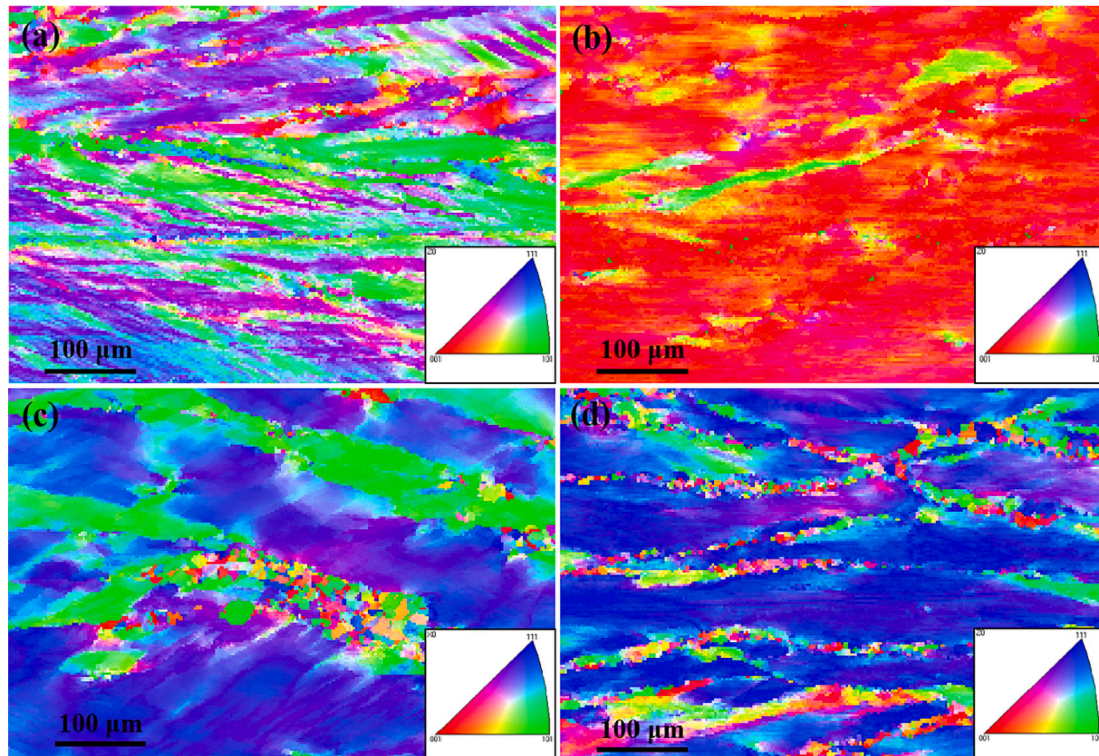

Fig. 6. EBSD micrographs of alloys deformed at 0.01 s⁻¹ strain rate: (a), (c) Cu-Sn-Ni-Zn-Ti 650 °C and 750 °C; (b), (d) Cu-Sn-Ni-Zn-Ti-Y 650 °C and 750 °C.
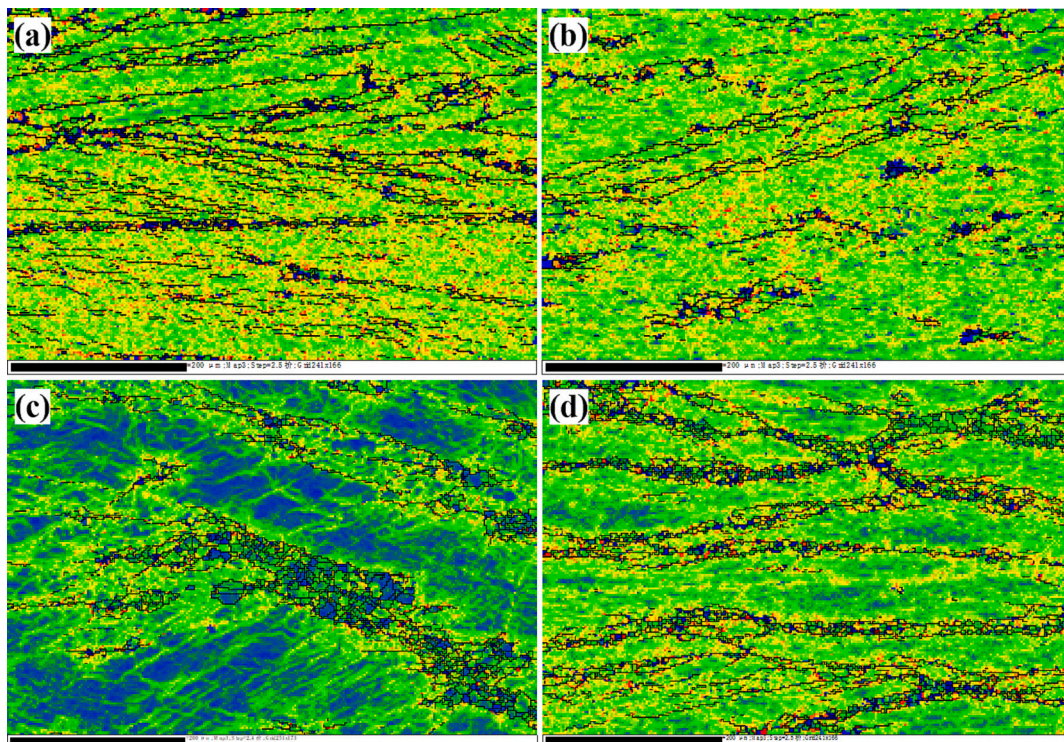
Fig. 7. The kernel average misorientation maps of (a) Cu-Sn-Ni-Zn-Ti 650 °C and 0.01 s^{-1}; (b) Cu-Sn-Ni-Zn-Ti-Y 650 °C and 0.01 s^{-1}; (c) Cu-Sn-Ni-Zn-Ti 750 °C and 0.01 s^{-1}; (d) Cu-Sn-Ni-Zn-Ti-Y 750 °C and 0.01 s^{-1}.

Fig. 8(a) and (b) show the orientation maps and misorientation angle distribution of the Cu-Sn-Ni-Zn-Ti and Cu-Sn-Ni-Zn-Ti-Y alloys deformed at 650 °C. The grain boundaries can be classified as low-angle grain boundaries ($\theta < 15°$) and high-angle grain boundaries ($\theta > 15°$) according to the orientation angle difference θ between adjacent grains' orientation. Based on the optical micrographs and stress-strain curves, it can be judged that the alloy is at the beginning stage of recrystallization at 650 °C. At this time, the number of large grains far exceeds the number of fine recrystallized grains, and high-angle grain boundaries dominate. Since Y promotes recrystallization, a small number of recrystallized grains appear inside the Cu-Sn-Ni-Zn-Ti-Y alloy. High-angle grain boundaries are closely related to recrystallization nucleation [33], and the conversion of high-angle grain boundaries to low-angle grain boundaries at the initial stage of recrystallization. The agglomeration of dislocations within the grain boundaries can form low-angle grain boundaries to provide energy for the nucleation of recrystallization. Therefore, the number of high-angle grain boundaries decreases, and the number of low-angle grain boundaries increases in the Cu-Sn-Ni-Zn-Ti-Y alloy.

The increase in temperature promotes the migration of high-angle grain boundaries, which consumes dislocations, reduces the number of low-angle grain boundaries, and forms equiaxed crystals with a small number of dislocations [34]. As seen in Fig. 8(c) and (d), recrystallization is commonly formed within the alloy at 750 °C. The percentage of high-angle grain boundaries increases significantly for both alloys with deformation temperature. The Cu-Sn-Ni-Zn-Ti-Y alloy has a higher percentage of high-angle grain boundaries under the same deformation conditions, which means that the Y addition promotes recrystallization.

To investigate the texture evolution in the Cu-Sn-Ni-Zn-Ti and Cu-Sn-Ni-Zn-Ti-Y alloys during hot deformation, the pole figures of the two alloys deformed at 0.01 s^{-1} strain rate and different temperatures were observed. It can be seen comparing Fig. 9(a) and (b), that the texture of the alloy deformed at 650 °C changes from the {011}<112 > Brass texture to the {001}<100 > Cube texture after the addition of Y. Fig. 9 (a) and (c) show that the texture of the Cu-Sn-Ni-Zn-Ti alloy changes

from the {011}<112 > Brass texture to the {111}<211 > R texture after increasing the deformation temperature from 650 °C to 750 °C. The addition of Y at the 750 °C deformation temperature decreased the texture strength from 21.83 to 12.82, indicating that Y reduced the texture strength of the Cu-Sn-Ni-Zn-Ti alloy [22].

3.5. Precipitates

The hot deformation experiments are mainly used to investigate the high-temperature deformation behavior of materials, as well as the deformation mechanism and microstructure evolution. In order to analyze the microstructure at a smaller scale, TEM characterization was performed. The stress concentrates near the grain boundaries and microcracks during hot deformation due to thermal and microstructure evolution stresses, accompanied by the generation of a large number of dislocations. As seen in Fig. 10(a) and (b), many deformation microstructure features appear inside the alloy: sub-grain boundaries, dislocation tangles, deformation bands, etc. A large number of dislocations are gathered and tangled together forming dislocation cells. Dislocations are mostly generated at grain boundaries and defects, while they rarely appear inside the grains. At the same time, a large number of distributed precipitated phases appear in the copper matrix to impede the dislocation movement. These precipitated phases are spread around the sub-grain boundaries and dislocation lines, which creates a pegging effect of precipitation on dislocations. The pinned spots inhibit dislocation slip while deformation bands, tangles, and secondary phase particles interact and become intrinsic to the elevated flow stress of the alloy [35].

In Fig. 10(c) the precipitated phases are mostly spherical and rod-like. It is well documented that at high strains the precipitated phases are mainly rod and spherical, and at low strains, some regions produce needle-like precipitated phases [36,37]. The yellow region in Fig. 10(c) shows a precipitated phase with a diameter of about 80 nm. The calibration of its diffraction spot shows that this precipitated phase is Cu$_4$Ti with lattice parameters of a = 4.53 nm, b = 4.342 nm, c = 12.93 nm, and
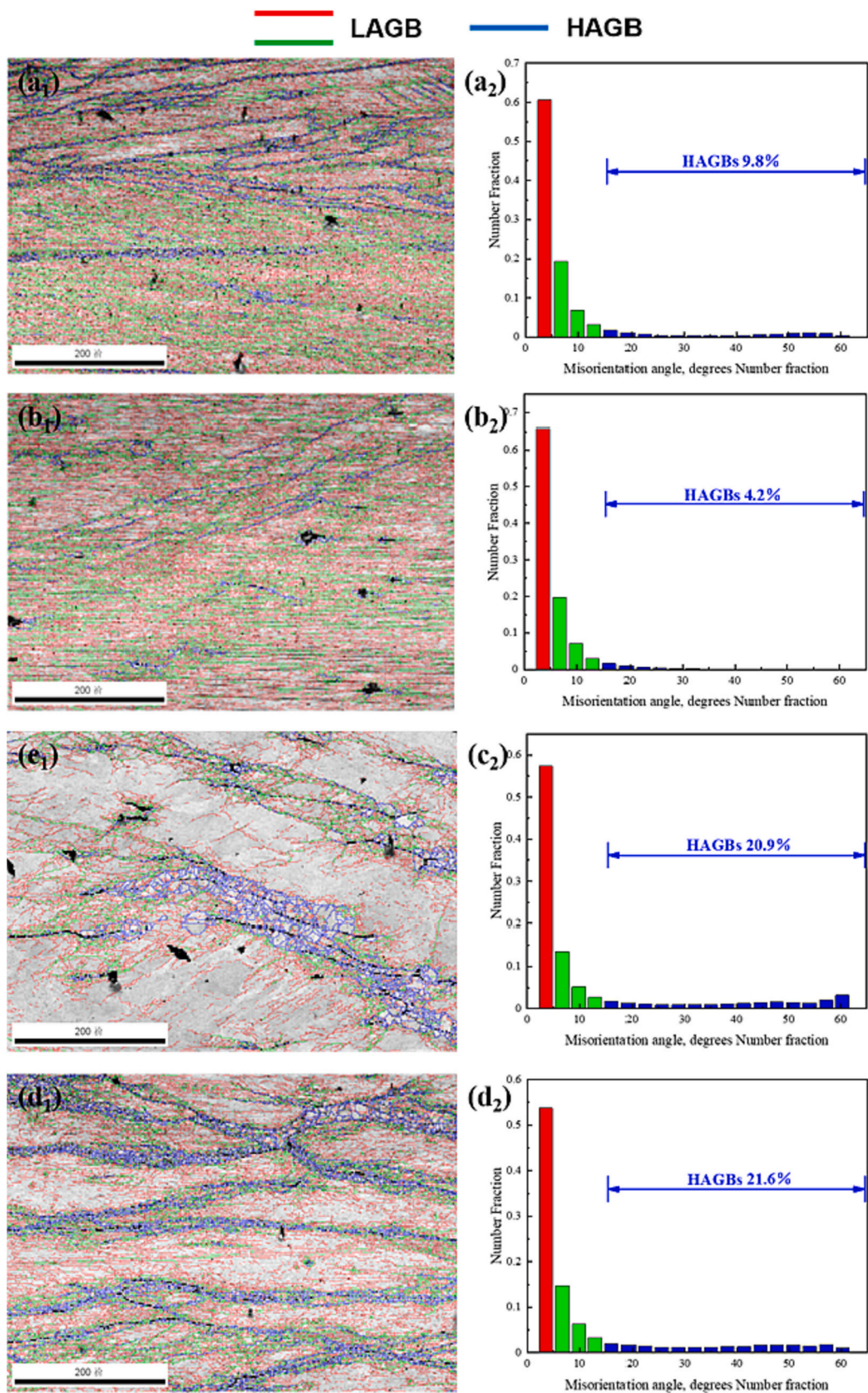
Fig. 8. EBSD orientation maps and misorientation angles distributions of alloys deformed at 0.01 s^{-1} strain rate and different temperatures: (a$_1$), (a$_2$) Cu-Sn-Ni-Zn-Ti 650 °C; (b$_1$), (b$_2$) Cu-Sn-Ni-Zn-Ti-Y 650 °C; (c$_1$), (c$_2$) Cu-Sn-Ni-Zn-Ti 750 °C; (d$_1$), (d$_2$) Cu-Sn-Ni-Zn-Ti-Y 750 °C.

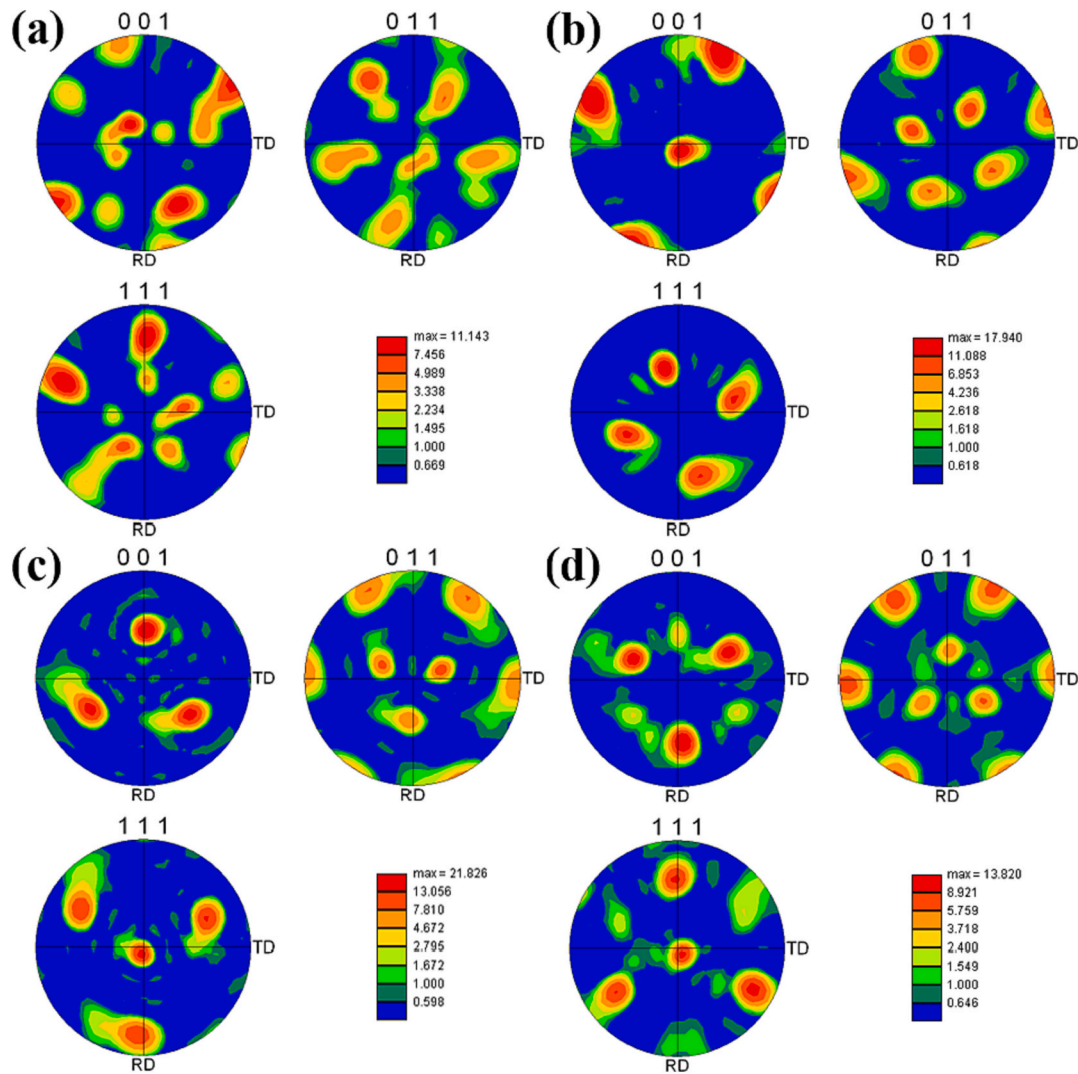**Fig. 9.** Pole figures of alloys deformed at 0.01 s^{-1} strain rate and different temperatures: (a) Cu-Sn-Ni-Zn-Ti 650 °C; (b) Cu-Sn-Ni-Zn-Ti-Y 650 °C; (c) Cu-Sn-Ni-Zn-Ti 750 °C; (d) Cu-Sn-Ni-Zn-Ti-Y 750 °C.

α = β = γ = 90°, as seen in Fig. 10(e). Fig. 10(d) shows an enlarged view of the blue region in Fig. 10(e) with the crystalline band axes of [100] and [0$\bar{1}$1] for the Cu$_4$Ti and copper matrix, respectively. Humphreys et al. [38] found that the size of the precipitated phase affects the mechanical properties, crystal structure, and texture of the material. Recrystallization is more likely to occur when the size of the precipitated phase is in the 0.5–2 μm range. When the precipitated phase size is <0.5 μm, a pegging effect occurs, which hinders dislocation movement and is not conducive to recrystallization; in other words, it inhibits dynamic recrystallization. The optical micrographs and IPF maps of the Cu-Sn-Ni-Zn-Ti alloy show a low degree of recrystallization at 650 °C, thus verifying that the pegging effect of the small-sized precipitated phase inhibits recrystallization. The inverse fast Fourier transform (IFFT) of the diffraction spots after the fast Fourier transform (FFT) of the high-resolution map of the precipitated Cu$_4$Ti phase was calculated to obtain the crystallographic spacing d = 0.2164 nm for the (020) crystalline surface.

Fig. 11(a) shows the TEM micrograph of the Cu-Sn-Ni-Zn-Ti alloy. The size of the precipitated phase in the figure is 70.84 nm × 77.85 nm. The analysis of the diffraction spot can be concluded that the precipitated phase is Cu$_4$Ti phase. Fig. 11(c) and (d) show the EDS results. It is known that Ni can be infinitely miscible in Cu, and some Ni atoms replace Cu atoms to form alloyed Cu$_4$Ti. The number of (Cu, Ni)/Ti

atoms in the precipitates is 4, which further proves that the precipitated phase is Cu$_4$Ti. Fig. 11(e) shows the XRD spectra of the Cu-Sn-Ni-Zn-Ti alloy. The diffraction reflections appear near 42°, 45°, and 48°, corresponding to the Cu$_4$Ti phase formed in the alloy.

3.6. DRX mechanism

In order to investigate the internal microstructure changes during hot deformation, three stages of work hardening, dynamic reversion (DRV), and dynamic recrystallization (DRX) were analyzed by combining the stress-strain curve and TEM images in Fig. 12. In the pre-deformation stage, the alloy is suddenly deformed so that the internal atoms do not have time to diffuse, and the dislocation density increases dramatically and dislocations appear in large numbers at grain boundaries and defects. Dislocations start to entangle and form dislocation cells. At this time, work hardening is still dominant and the rheological stress increases rapidly. As the strain increases, the alloy begins to deform uniformly and the dislocation cells gradually transform into sub-grain boundaries. The higher deformation temperature provides the conditions for dynamic recovery, and the dislocations slip, climb, and cancel each other to reduce the dislocation density, which is the dynamic recovery stage. Finally, the sub-crystal transforms into a high-angle grain boundary by rotation. High-angle grain boundaries have a
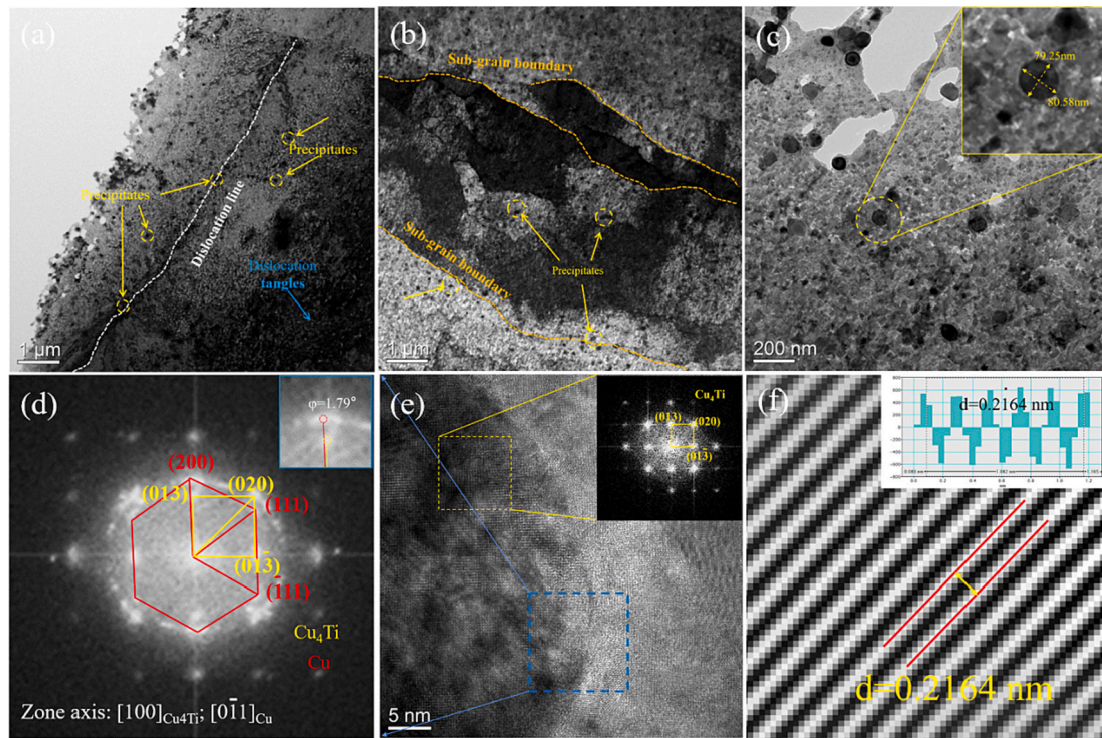
Fig. 10. Microstructure of the Cu-Sn-Ni-Zn-Ti alloy deformed at 650 °C and 0.01 s^{-1}: (a), (b), (c) TEM micrographs; (d) SADP of blue rectangle area in (e); (e) HRTEM; (f) measurement of crystal spacing. (For interpretation of the references to colour in this figure legend, the reader is referred to the web version of this article.)
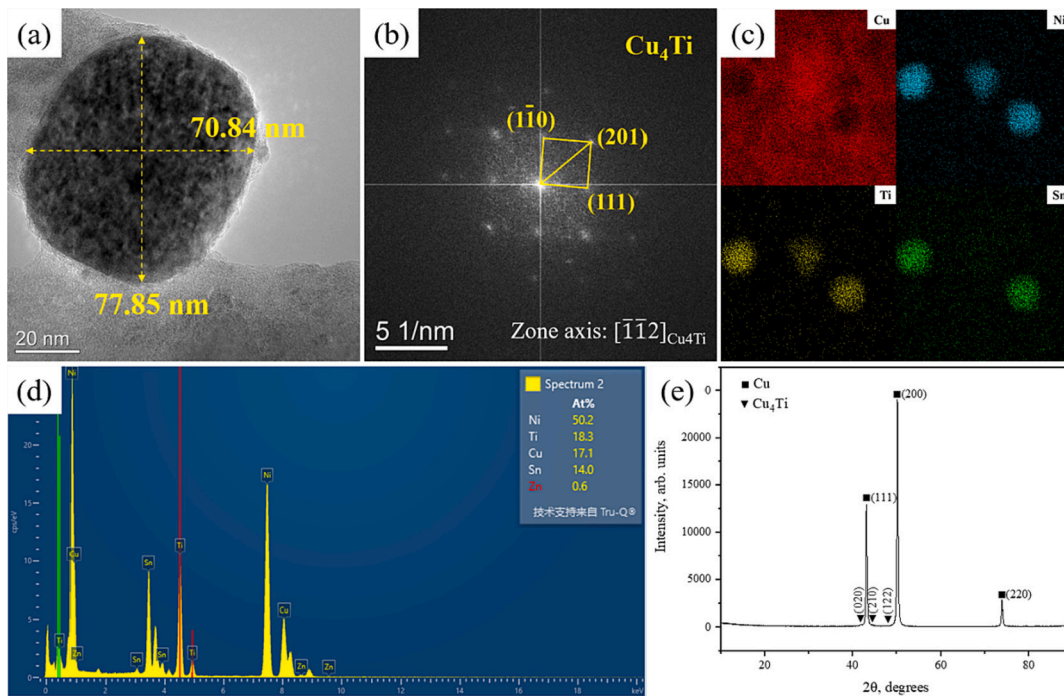

Fig. 11. Cu-Sn-Ni-Zn-Ti alloy deformed at 650 °C and 0.01 s^{-1}. (a) TEM micrograph; (b) SADP of (a); (c) EDS maps; (d) EDS result; (e) XRD spectra.

higher migration rate and can be rapidly transformed into recrystallized nuclei, resulting in the formation of new recrystallized grains, which is a typical continuous dynamic recrystallization mechanism [39,40]. On the other hand, dislocations are rearranged at grain boundaries, which form sub-grains by continuously engulfing the surrounding sub-crystals and finally forming recrystallized grains. This process corresponds to the

discontinuous dynamic recrystallization mechanism [41]. Therefore, the two main recrystallization mechanisms for the Cu-Sn-Ni-Zn-Ti alloys are CDRX and DDRX.
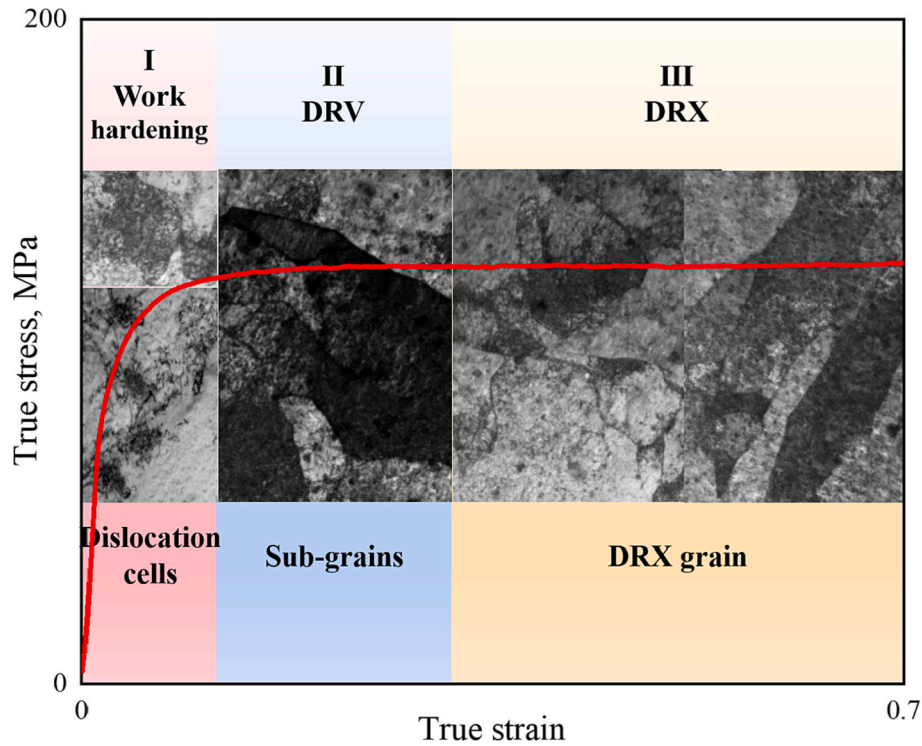
Fig. 12. Schematic illustration of the true stress-strain curves and the corresponding DRX mechanisms for copper alloy deformed at 650 °C and 0.01 s^{-1} strain rate.

3.7. Processing maps

Copper alloys were subject to deformation and cracking during thermal processing. In order to obtain suitable processing conditions and reduce material losses, the processing maps were constructed using a dynamic material model (DMM). The total power P of the system is divided into two parts, denoted by G and J, as described in Eq. (13) [42]:

$$P = G + J = \sigma\dot{\varepsilon} = \int_0^{\dot{\varepsilon}} \sigma d\dot{\varepsilon} + \int_0^{\sigma} \dot{\varepsilon} d\sigma \qquad (13)$$

The strain rate sensitivity parameter m is defined as:

$$m = \frac{dJ}{dG} = \left(\frac{\partial ln\sigma}{\partial ln\dot{\varepsilon}}\right)_{\dot{\varepsilon},T} \qquad (14)$$

Under ideal conditions, J reaches its maximum value when m = 1.

$$J_{max} = \frac{\sigma\dot{\varepsilon}}{2} = \frac{P}{2} \qquad (15)$$

Here, G represents the power dissipation due to plastic deformation, and J is the power dissipation associated with the change of microstructure. When J reaches its maximum value, the power dissipation efficiency η can be defined as:

$$\eta = \frac{J}{J_{max}} = \frac{2m}{2m+1} \qquad (16)$$

The power dissipation map is formed by η, T and $\dot{\varepsilon}$. Higher η values imply that higher energy is required for dynamic recrystallization and better mechanical properties of the alloy can be obtained after thermal processing. Meanwhile, based on the extreme value principle of irreversible thermodynamics, the rheological instability criterion equation can be expressed as in [42]:

$$\xi(\dot{\varepsilon}) = \frac{\partial ln\left(\frac{m}{m+1}\right)}{\partial ln\dot{\varepsilon}} + m < 0 \qquad (17)$$

The region with a negative calculated value is the rheological instability region, and the positive value is the safe region so that the instability map of thermal processing can be obtained. The instability and the power dissipation maps are superimposed to obtain the hot processing map of the alloy. Fig. 13 shows the processing maps of the Cu-Sn-Ni-Zn-Ti and Cu-Sn-Ni-Zn-Ti-Y alloys deformed to a true strain of 0.1 and 0.3, respectively. The black shaded area in the figure indicates the unstable region, and the other regions are safe. The optimal processing region for the Cu-Sn-Ni-Zn-Ti alloy is 650–950 °C with a strain rate of 0.01–0.6 s^{-1}. The optimal processing region for the Cu-Sn-Ni-Zn-Ti-Y alloy is 700–950 °C with a strain rate of 0.001–0.3 s^{-1}. It is noteworthy that the unstable region of the alloy is reduced with the addition of Y, which makes it more suitable for processing at low strain rates.

4. Conclusions

The hot deformation experiments of the Cu-Sn-Ni-Zn-Ti and Cu-Sn-Ni-Zn-Ti-Y alloys were carried out using a Gleeble-1500 simulator at 550–950 °C deformation temperatures and 0.001–10 s^{-1} strain rates. The effects of Y addition on the microstructure evolution of the alloys were investigated. Several conclusions can be drawn:

(1) Y addition can promote the recrystallization of the Cu-Sn-Ni-Zn-Ti alloy.

(2) The constitutive equations of the Cu-Sn-Ni-Zn-Ti and Cu-Sn-Ni-Zn-Ti-Y alloys were obtained. The hot deformation activation energy of the two alloys was calculated to be 274.855 kJ/mol and 307.757 kJ/mol, respectively, and the addition of Y increased the hot deformation activation energy of the alloys by 12%.

(3) The microstructure of the Cu-Sn-Ni-Zn-Ti and Cu-Sn-Ni-Zn-Ti-Y alloys was analyzed by EBSD. The texture of the Cu-Sn-Ni-Zn-Ti alloy deformed at 650 °C and 750 °C was the {011}<112 > Brass texture and the {111}<211 > R texture, and the texture of Cu-Sn-Ni-Zn-Ti-Y alloy was the {001}<100 > Cube texture and the {111}<211 > R texture. It is noteworthy that the texture types of the two alloys deformed at 750 °C did not change, but the texture strength decreased.
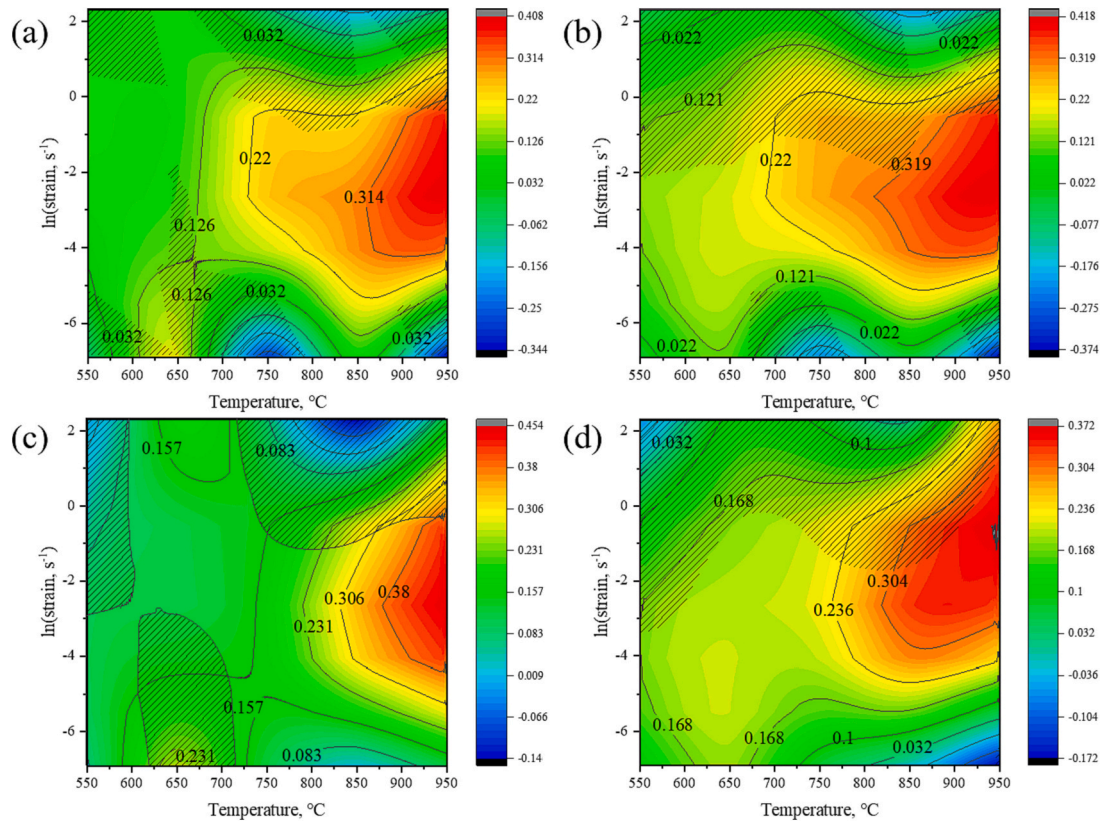
Fig. 13. Processing maps under different strains. Cu-Sn-Ni-Zn-Ti alloy: (a) ε = 0.1, (b) ε = 0.3; Cu-Sn-Ni-Zn-Ti-Y alloy: (c) ε = 0.1, (d) ε = 0.3.

(4) TEM analysis of the Cu-Sn-Ni-Zn-Ti alloy revealed the small-sized Cu$_4$Ti precipitated phase, which can peg dislocations and grain boundaries.

(5) The recrystallization mechanism of the Cu-Sn-Ni-Zn-Ti alloy was analyzed by obtaining compression stress-strain curves and TEM characterization. The CDRX and DDRX mechanisms are the main DRX mechanisms of the Cu-Sn-Ni-Zn-Ti alloy.

(6) The best processing region for the Cu-Sn-Ni-Zn-Ti alloy is 650–950 °C and 0.01–0.6 s^{-1} strain rate. The best processing region for the Cu-Sn-Ni-Zn-Ti-Y alloy is 700–950 °C with a 0.001–0.3 s^{-1} strain rate.

Declaration of Competing Interest

The authors declare that they have no known competing financial interests or personal relationships that could have appeared to influence the work reported in this paper.

Data availability

No data was used for the research described in the article.

Acknowledgments

References

[1] K.X. Song, Y.F. Geng, Y.J. Ban, Y. Zhang, Z. Li, X.J. Mi, J. Cao, Y.J. Zhou, X. B. Zhang, Effects of strain rates on dynamic deformation behavior of Cu-20Ag alloy, J. Mater. Sci. Technol. 79 (2021) 75–87, https://doi.org/10.1016/j.jmst.2020.11.043.

[2] A.K. Shukla, S.V.S. Narayana Murty, S.C. Sharma, K. Mondal, Constitutive modeling of hot deformation behavior of vacuum hot pressed Cu-8Cr-4Nb alloy, Mater. Design 75 (2015) 57–64, https://doi.org/10.1016/j.matdes.2015.03.023.

[3] J. Li, G.J. Huang, X.J. Mi, L.J. Peng, H.F. Xie, Y.L. Kang, Microstructure evolution and properties of a quaternary Cu–Ni–Co–Si alloy with high strength and conductivity, Mater. Sci. Eng. A 776 (2019), https://doi.org/10.1016/j.msea.2019.138390, 138390.

[4] I. Solodkyi, O. Bezdorozhev, P. Loboda, High electrical conductive copper matrix composites reinforced with LaB6–TiB2 eutectic particles, Vacuum. 177 (2020), 109407, https://doi.org/10.1016/j.vacuum.2020.109407.

[5] Y.J. Ban, Y. Zhang, B.H. Tian, K.X. Song, M. Zhou, X.H. Zhang, Y.L. Jia, X. Li, Y. F. Geng, Y. Liu, A.A. Volinsky, EBSD analysis of hot deformation behavior of cu-Ni-co-Si-Cr alloy, Mater. Charact. 169 (2020), 110656, https://doi.org/10.1016/j.matchar.2020.110656.

[6] Z.M. Li, Z.L. Cheng, X.N. Li, Y.L. Hu, N.J. Li, Y.H. Zheng, Y.Y. Shao, R.W. Liu, C. Dong, Enthalpic interaction promotes the stability of high elastic cu-Ni-Sn alloys, J. Alloys Compd. 896 (2021), 163068, https://doi.org/10.1016/j.jallcom.2021.163068.

[7] J. Wang, W.L. Zhou, J. Li, M. Brochu, Y.F. Zhao, Microstructures and properties of SLM-manufactured cu-15Ni-8Sn alloy, Addit. Manuf. 31 (2020), 100921, https://doi.org/10.1016/j.addma.2019.100921.

[8] M. Miki, Y. Ogino, Effects of doped elements on the cellular precipitation in Cu–10Ni–8Sn alloy, Mater. Trans. JIM 35 (5) (2007) 313–318, https://doi.org/10.2320/matertrans1989.35.313.

[9] R. Monzen, C. Watanabe, Microstructure and mechanical properties of Cu–Ni–Si alloys, Mater. Sci. Eng. A 483–484 (2008) 117–119, https://doi.org/10.1016/j.msea.2006.12.163.

[10] W.N. Liao, X.F. Liu, Y.H. Yang, S.Q. Wang, M. Du, Effect of cold rolling reduction rate on mechanical properties and electrical conductivity of Cu–Ni–Si alloy prepared by temperature controlled mold continuous casting, Mater. Sci. Eng. A 763 (2019) 138, https://doi.org/10.1016/j.msea.2019.138068.

[11] C. Guo, J. Wan, J. Chen, X. Xiao, H. Huang, J. Liu, B. Yang, Inhibition of discontinuous precipitation and enhanced properties of Cu-15Ni-8Sn alloy with Fe addition, Mater. Sci. Eng. A 795 (2020), 139917, https://doi.org/10.1016/j.msea.2020.139917.

[12] Y.F. Geng, X. Li, H.L. Zhou, Y. Zhang, Y.L. Jia, B.H. Tian, Y. Liu, A.A. Volinsky, X. H. Zhang, K.X. Song, G.X. Wang, L.H. Li, J.R. Hou, Effect of Ti addition on

microstructure evolution and precipitation in Cu–Co–Si alloy during hot deformation, J. Alloys Compd. 821 (2019), 153518, https://doi.org/10.1016/j.jallcom.2019.153518.

[13] J.Y. Cheng, B. Shen, F.X. Yu, Precipitation in a cu–Cr–Zr–mg alloy during aging, Mater. Charact. 81 (2013) 68–75, https://doi.org/10.1016/j.matchar.2013.04.008.

[14] S. Xu, H.D. Fu, Y.T. Wang, J.X. Xie, Effect of ag addition on the microstructure and mechanical properties of cu-Cr alloy, Mater. Sci. Eng. A 726 (2018) 208–214, https://doi.org/10.1016/j.msea.2018.04.077.

[15] Z. Zhao, Y. Zhang, B.H. Tian, Y.L. Jia, Y. Liu, K.X. Song, Alex A. Volinsky, Co effects on Cu-Ni-Si alloys microstructure and physical properties, J. Alloys Compd. 797 (2019) 1327–1337, https://doi.org/10.1016/j.jallcom.2019.05.135.

[16] Y. Zhang, A.A. Volinsky, H.T. Tran, Z. Chai, P. Liu, B.H. Tian, Y. Liu, Aging behavior and precipitates analysis of the Cu-Cr-Zr-Ce alloy, Mater. Sci. Eng. A 650 (2016) 248–253, https://doi.org/10.1016/j.msea.2015.10.046.

[17] V. Renganathan, R. Balaji, S.M. Chen, T.W. Chen, M.A. Ali, F. Al-Hemaid, M.S. El-Shikh, Bimetallic multifunctional nanostructures based on Cu–Ni alloy for environmental sensing and catalysis applications, Vacuum. 184 (2020), 109845, https://doi.org/10.1016/j.vacuum.2020.109845.

[18] J.C. Zhao, M.R. Notis, Spinodal decomposition, ordering transformation, and discontinuous precipitation in a Cu-15Ni-8Sn alloy, Acta Mater. 46 (12) (1998) 4203–4218, https://doi.org/10.1016/S1359-6454(98)00095-0.

[19] B.J. Wang, Y. Zhang, B.H. Tian, V. Yakubov, J.C. An, Alex A. Volinsky, Y. Liu, K.X. Song, L.H. Li, M. Fu, Effects of Ce and Y addition on microstructure evolution and precipitation of Cu-Mg alloy hot deformation, J. Alloys Compd. 781 (2019) 118–130, https://doi.org/10.1016/j.jallcom.2018.12.022.

[20] L.L. Yuan, W. Wang, X.M. Huang, Y.F. Qi, X.Y. Li, Joining of Al$_2$O$_3$ to Cu with Cu-Sn-Ti active brazing filler alloy, Weld World. 66 (2022) 1471–1479, https://doi.org/10.1007/s40194-022-01305-5.

[21] X.F. Wang, M.X. Guo, J.R. Luo, J. Zhu, J.S. Zhang, L.Z. Zhuang, Effect of Zn on microstructure, texture and mechanical properties of Al-Mg-Si-Cu alloys with a medium number of Fe-rich phase particles, Mater. Charact. 134 (2017) 123–133, https://doi.org/10.1016/j.matchar.2017.10.012.

[22] P.F. Yang, M. Zhou, Y. Zhang, Y.L. Jia, B.H. Tian, Y. Liu, A.A. Volinsky, Effect of Y addition on microstructure evolution and precipitation of Cu-Co-Si alloy during hot deformation, Mater. Charact. 181 (2021), 111502, https://doi.org/10.1016/j.matchar.2021.111502.

[23] J.B. Correia, H.A. Davies, C.M. Sellars, Strengthening in rapidly solidified age hardened CuCr and CuCrZr alloys, Acta Mater. 45 (1997) 177–190, https://doi.org/10.1016/S1359-6454(96)00142-5.

[24] H. Khodashenas, H. Mirzadeh, M. Malekan, M. Emamy, Constitutive modeling of flow stress during hot deformation of Sn-Al-Zn-Cu-Mg multi-principal-element alloy, Vacuum. 170 (2019), 108970, https://doi.org/10.1016/j.vacuum.2019.108970.

[25] Z.Y. Ding, S.G. Jia, P.F. Zhao, M. Deng, K.X. Song, Hot deformation behavior of Cu-0.6Cr-0.03Zr alloy during compression at elevated temperatures, Mater. Sci. Eng. A 570 (2013) 87–91, https://doi.org/10.1016/j.msea.2013.01.059.

[26] R. Mishnev, I. Shakhova, A. Belyakov, R. Kaibyshev, Deformation microstructures, strengthening mechanisms, and electrical conductivity in a Cu-Cr-Zr alloy, Mater. Sci. Eng. A 629 (2015) 29–40, https://doi.org/10.1016/j.msea.2015.01.065.

[27] Y. Wang, X.M. Qiu, D.Q. Sun, S.Q. Yin, Influence of Ti on microstructure and strength of c-BN/ Cu–Ni–Sn–Ti composites, Int. J. Refract. Met. Hard Mater. 29 (2) (2011) 293–297, https://doi.org/10.1016/j.ijrmhm.2010.12.004.

[28] C.M. Sellars, W.J. McTegart, On the mechanism of hot deformation, Acta Metall. 14 (1966) 1136–1138, https://doi.org/10.1016/0001-6160(66)90207-0.

[29] Z. Savaedi, R. Motallebi, H. Mirzadeh, A review of hot deformation behavior and constitutive models to predict flow stress of high-entropy alloys, J. Alloys Compd. 903 (2022), 163964, https://doi.org/10.1016/j.jallcom.2022.163964.

[30] R. Motallebi, Z. Savaedi, H. Mirzadeh, Additive manufacturing - a review of hot deformation behavior and constitutive modeling of flow stress, Curr. Opin. Solid State Mater. Sci. 26 (2022), 100992, https://doi.org/10.1016/j.cossms.2022.100992.

[31] Y.S. Wu, X.Z. Qin, C.S. Wang, L.Z. Zhou, Influence of phosphorus on hot deformation microstructure of a Ni-Fe-Cr based alloy, Mater. Sci. Eng. A 768 (2019) 138454, https://doi.org/10.1016/j.msea.2019.138454.

[32] W.J. He, A. Chapuis, X. Chen, Q. Liu, Effect of loading direction on the deformation and annealing behavior of a zirconium alloy, Mater. Sci. Eng. A 734 (2018) 364–373, https://doi.org/10.1016/j.msea.2018.08.013.

[33] A. Heidarzadeh, T. Saeid, V. Klemm, A. Chabok, Y.T. Pei, Effect of stacking fault energy on the restoration mechanisms and mechanical properties of friction stir welded copper alloys, Mater. Design 162 (2019) 185–197, https://doi.org/10.1016/j.matdes.2018.11.050.

[34] K. Huang, K. Marthinsen, Q.L. Zhao, R.E. Loge, The double-edge effect of second-phase particles on the recrystallization behaviour and associated mechanical properties of metallic materials, Prog. Mater. Sci. 92 (2018) 284–359, https://doi.org/10.1016/j.pmatsci.2017.10.004.

[35] M.Y. Li, H. Wang, Y.H. Guo, H.L. Wang, D.D. Zheng, J.F. Shan, Y.Q. Chang, Microstructures and mechanical properties of the novel CuCrZrFeTiY alloy for fusion reactor, J. Nucl. Mater. 532 (2020), 152063, https://doi.org/10.1016/j.jnucmat.2020.152063.

[36] J. Li, G.J. Huang, X.J. Mi, L.J. Peng, H.F. Xie, Y.L. Kang, Effect of Ni/Si mass ratio and thermomechanical treatment on the microstructure and properties of cu-Ni-Si alloys, Materials. 12 (13) (2019) 2076, https://doi.org/10.3390/ma12132076.

[37] Y.L. Jia, M.P. Wang, C. Chen, Q.Y. Dong, S. Wang, Z. Li, Orientation and diffraction patterns of d-Ni2Si precipitates in cu-Ni-Si alloy, J. Alloys Compd. 557 (2013) 147–151, https://doi.org/10.1016/j.jallcom.2012.12.154.

[38] F.J. Humphreys, P.N. Kalu, Dislocation-particle interactions during high temperature deformation of two-phase aluminum alloys, Acta Metall. 35 (1987) 2815–2829, https://doi.org/10.1016/0001-6160(87)90281-1.

[39] W.L. Cheng, Y. Bai, S.C. Ma, L.F. Wang, H.X. Wang, H. Yu, Hot deformation behavior and workability characteristic of a fine-grained mg-8Sn-2Zn-2Al alloy with processing map, J. Mater. Sci. Technol. 35 (2019) 1198–1209, https://doi.org/10.1016/j.jmst.2018.12.001.

[40] Q.Y. Zhao, F. Yang, R. Torrens, L. Bolzoni, Comparison of hot deformation behaviour and microstructural evolution for Ti-5Al-5V-5Mo-3Cr alloys prepared by powder metallurgy and ingot metallurgy approaches, Mater. Design 169 (2019), 107682, https://doi.org/10.1016/j.matdes.2019.107682.

[41] D. Jia, W.R. Sun, D.S. Xu, F. Liu, Dynamic recrystallization behavior of GH4169G alloy during hot compressive deformation, J. Mater. Sci. Technol. 35 (2019) 1851–1859, https://doi.org/10.1016/j.jmst.2019.04.018.

[42] J. Yang, G. Wang, X. Jiao, Y. Li, Q. Liu, High-temperature deformation behavior of the extruded Ti-22Al-25Nb alloy fabricated by powder metallurgy, Mater. Charact. 137 (2018) 170–179, https://doi.org/10.1016/j.matchar.2018.01.019.